doi:10.20944/preprints202211.0334.v1

*Article*

# Optimal Icosahedral Copper-based Bimetallic Clusters for the Selective Electrocatalytic $CO_2$ Conversion to One Carbon Products

**Azeem Ghulam Nabi,**[*1,2,3,5] **Aman-ur-Rehman,**[2,4] **Akhtar Hussain,**[5] **Gregory A. Chass** [1,6,7] **and Devis Di Tommaso,**[*1]

[1] Department of Chemistry, School of Physical and Chemical Sciences, Queen Mary University of London, Mile End Road, London, E1 4NS, United Kingdom
[2] Department of Physics and Applied Mathematics, Pakistan Institute of Engineering and Applied Sciences, P. O. 45650, Nilore, Islamabad, Pakistan
[3] Department of Physics, University of Gujrat, Jalalpur Jattan Road, Gujrat, Pakistan
[4] Department of Nuclear Engineering, Pakistan Institute of Engineering & Applied Sciences, P.O. 45650, Nilore, Islamabad, Pakistan
[5] Theoretical Physics Division, Pakistan Institute of Nuclear Engineering & Technology (PINSTECH), Islamabad, Pakistan
[6] Department of Chemistry, McMaster University, Hamilton, Ontario, L8S 4L8, Canada
[7] Faculty of Land and Food Systems, The University of British Columbia, Vancouver BC, V6T1Z4, Canada
* Correspondence: g.azeem@qmul.ac.uk, d.ditommaso@qmul.ac.uk;

**Abstract:** The electrochemical $CO_2$ reduction reaction can lead to high value-added molecules production while helping decrease anthropogenic $CO_2$ emissions. Copper can reduce $CO_2$ to more than thirty different hydrocarbons and oxygenates, but it lacks the required selectivity. We present a computational investigation of the role of nano-structuring and alloying in Cu-based catalysts on the activity and selectivity of $CO_2$ reduction to one-carbon products: carbon monoxide, formic acid, formaldehyde, methanol, and methane. The adsorption, activation, and conversion of $CO_2$ were computed on monometallic and bimetallic (decorated and core-shell) 55-atom Cu-based clusters. The dopant metals considered were Ag, Cd, Pd, Pt, and Zn, located at different coordination sites. The relative binding strength of the intermediates at different applied potentials were used to identify the optimal catalyst for the selective $CO_2$ conversion to one carbon products. It was discovered that single atom doping with Cd and Zn is optimal for the $CO_2$ to carbon monoxide conversion. The core-shell models with Ag, Pd, and Pt provided higher selectivity for formic acid and formaldehyde. The Cu-Pt and Cu-Pd showed lowest overpotential for methane formation.

**Keywords:** $CO_2$ reduction; copper catalysts; metal doping; density functional calculations

## 1. Introduction

The rising carbon dioxide ($CO_2$) level in the atmosphere due to fossil fuel combustion, a major cause of global warming, poses a serious threat to humankind. One of the most promising solutions is the chemical conversion of $CO_2$ into value-added chemicals and materials.[1] The electrochemical $CO_2$ reduction reaction (e$CO_2$RR) has emerged as a potential strategy for converting $CO_2$ because if coupled with electricity from renewable sources (wind, solar, or hydropower plants), the e$CO_2$RR could achieve a carbon-neutral energy cycle.[2,3] The main challenges in e$CO_2$RR lie in the activation of $CO_2$ minimizing competitive pathways such as the hydrogen evolution reaction (HER, $H^+ + e^- \rightarrow \frac{1}{2} H_2$) [4,5] and the conversion of $CO_2$ to a specific product with good selectivity, given the marginal difference in the electrochemical potentials of $CO_2$ reduction into different products.[2] For example, $CO_2$ to ethylene is –0.34 V while to methanol is –0.38 V, against the standard hydrogen electrode.[6]

Catalysts can facilitate favorable pathways to reduce the overall energy requirements of e$CO_2$RR. Due to their ability to activate $CO_2$, early research focused on noble metal-based catalysts (Pt, Rh, Ir),[7–11] yet their scarcity and cost have hampered development. Hence, earth abundant and active metal-based catalysts are needed to develop a sustainable solution to $CO_2$ transformation. Copper (Cu) is the best candidate for e$CO_2$RR, being the only metal surface that reduces $CO_2$ to more than thirty hydrocarbons and oxygenates [12] , but it lacks the required selectivity.[13–15] Relevant studies dedicated to improving selectivity and hindering the HER have investigated the adsorption/desorption mechanism on single crystal Cu electrodes to demonstrate the role of surface morphology[16]. It was discovered that Cu crystal facets with high index planes such as Cu(711) are more selective to valuable C2 products, such as ethylene and methanol, than the dominant Cu(111) surface,[17] while stepped Cu surfaces such as the (211) facet can easily produce C1 hydrocarbons.[18] Computational studies also revealed that the higher activity of polycrystalline Cu nanoparticles is due to the presence of stepped facets, such as (110),[19] (211)[20] and Cu(321).[21] These stepped surfaces occur in metal clusters,[17,21–23] where both the number of uncoordinated sites at the corners and edges[24] and the surface-to-volume ratio of nanoparticles are higher than those on copper surfaces, which may lead to improved catalytic properties towards e$CO_2$RR.[12]

Another strategy to improve the activity and selectivity of Cu electrodes is metal (M) doping.[13] Bimetallic catalysts often show better catalytic performance than the corresponding elemental metal ones due to synergic effects.[25] The dopant provides reaction sites with varied electronic properties and modifies those of the host (Cu), influencing the adsorption strength of the intermediates of the e$CO_2$RR. Experimental studies also revealed that low doping concentration helps the formation of C1 products.[26,27] In particular, metal dopants such as Ag,[27,28] Cd,[29] Pd,[27,30] Pt,[31] and Zn[27,32] in Cu-M catalysts show efficiency towards C1/C2 products.

By combining nanoclusters and metal doping, Cu-based bimetallic nanoclusters could be efficient catalysts for e$CO_2$RR. In these systems, nano-structuring and metal-coupling can cooperate to enhance $CO_2$ activation and intermediate binding, effectively leading to specific product formation. In this regard, quantum mechanical modelling has provided insights into the structure, stability and catalytic properties of Cu-M clusters and demonstrated that an appropriate proportion of metal atoms influences the $CO_2$ activation and selectivity towards desired reactions. Using density functional theory (DFT) calculations, Alvarez-Garcia et al. investigated the binding and dissociation of $CO_2$ on four-atom bimetallic $Cu_nPd_{4-n}$ ($n$ = 0–4) clusters,[29] and found the ideal composition for adsorption energy and activation barrier was $Cu_3Pd$, in agreement with the Pd/(Pd + Cu) atomic ratio reported experimentally.[33,34] Investigation on the effect of substituting Cu with Zr in the four-atom $Cu_4$ cluster on $CO_2$ adsorption[35] revealed that the energy barriers for the direct dissociation of the $CO_2$ molecule to CO and O decreased significantly on bimetallic Cu−Zr clusters compared to that on pure $Cu_4$. Our recent computational work on small tetrahedral Cu-Sn cluster found the $Cu_2Sn_2$ system to suppress the competitive HER and was highly selective towards the electrochemical $CO_2$-to-CO conversion.[36] Xing et al. considered bimetallic $Pd_nCu_m$ ($m$ + n = 15 and $n > m$) clusters and showed $Pd_{10}Cu_5$ to have the best catalytic activity, particularly towards the $CO_2$ to COOH hydrogenation step.[30] Li et al. considered $(Cu)_n$ clusters with $n$ = 8, 20, 38 (even numbers) and $n$ = 13, 55 (odd numbers) to investigate the reactivity at the highly dense corner and edge sites and found the icosahedral $Cu_{55}$ to provide the lowest pathway to the CO intermediate and the C2 ethylene product.[24]

Theoretical calculations of clusters in the size range of $10 \leq n \leq 55$ showed that $(Cu)_n$ adopted the icosahedral structure[37]derived from the 13-atom icosahedron and the 55-atom icosahedron by adding or removing atoms. In addition, a comparison of icosahedral and cuboctahedral (n = 55, 147 and 309) clusters confirmed the icosahedral copper clusters to be more stable. Experimental verification of the formation of copper clusters using microemulsion technique revealed $Cu_{55}$ as one of the most abundant clusters followed by $Cu_{13}$, $Cu_{147}$ and $Cu_{309}$.[38] According to the recent research $Cu_{55}$ exhibits highly degenerate states,[39] which is a direct outcome of its icosahedral symmetry, as is validated by DFT calculations.

Therefore, study on nanoclusters such as the highly symmetric 55-atom icosahedral structures would give a deep understanding than stepped surfaces. This has been attributed to their larger surface-to-volume ratio and higher proportion of coordinatively unsaturated surface atoms (corner or edge) in comparison to bulk materials, resulting in a narrowing of the d-band, an upward shift of the band's energy, and consequently, a stronger adsorption of the reaction intermediates.[40] Investigation on the adsorption of $CO_2$ on icosahedral 55-atom Cu-based bimetallic clusters[41] found that for the $Cu_{55-x}Zr_x$ systems ( $x = 1–12$), the formation of the $CO_2$-activated state (linear to bent transition and elongation of C–O bonds) was endothermic on the pure copper cluster but barrierless and exothermic on the Zr-decorated system. Similarly, DFT calculations of $Cu_{55-x}Zr_x$ systems ($x = 0$, 12, 13, 42, 43 and 55) with a core@shell and decorated distribution of Cu and Ni atoms showed the presence of Ni on the clusters was crucial to the activation of $CO_2$.[42]

Although previous computational studies of icosahedral Cu-based bimetallic nanocatalysts considered the adsorption, activation and gas-phase dissociation of $CO_2$, in the context of $eCO_2RR$, the focus should be on the concerted proton-electron transfer (CPET) steps.[43]

Here, we present a computational investigation based on DFT calculations of the effect of nano-structuring and alloying in Cu-based catalysts on the activity and selectivity of the $eCO_2RR$. Starting from the icosahedral $Cu_{55}$ structure, we generated $Cu_{54}M_1$, $Cu_{43}M_{12}$ and $Cu_{30}M_{25}$decorated architectures and $Cu_{13}M_{42}$ core@shell model (M = Ag, Cd, Pd, Pt, and Zn) (**Figure 1**), with the metals located at three different coordination sites (6, 8 and 12). We provide a thorough analysis of the structural, thermodynamic and electronic properties of these nanoclusters and their ability to activate $CO_2$. The computational hydrogen electrode (CHE) model [44] is then applied to compute the mechanism of $eCO_2RR$ to carbon monoxide (CO), formic acid (HCOOH), formaldehyde ($CH_2O$), methane ($CH_4$) and methanol ($CH_3OH$). We compare the free energy profiles for the electrocatalytic $CO_2$ conversion to these C1 products to the competitive HER. The relative binding strength of the intermediates involved at different applied potentials is used to identify catalysts for the selective $CO_2$ conversion. For comparison purposes, calculations of the $eCO_2RR$ and HER were also conducted on the (100), (110), (111) and (211) facets of pure copper.

## 2. Computational methods

### *2.1. Atomistic models of clusters and surfaces*

The icosahedral ($I_h$) 55-atom monometallic Cu cluster was generated using the *ab initio* random searching AIRSS code.[45] The decorated $Cu_{54}M$ clusters were then generated by replacing one surface Cu with a dopant metal atom M, where M = Ag, Cd, Pd, Pt and Zn. As shown in **Figure 1(a)**, there are three possible coordination sites: CN6 (coordination number) is the edge site, CN8 is the corner site and CN12 is the centre of the nanocluster. The $Cu_{43}M_{12}$ model in **Figure 1(b)** was generated by replacing 12 Cu atoms with M located at CN6. The $Cu_{25}M_{50}$ model in **Figure 1(c)** was generated by replacing 12 Cu atoms with M located at CN8. The $Cu_{13}M_{42}$ core@shell model in **Fig. 1(d)** was generated by replacing all 13 surface Cu atoms with M. We also considered four-layer (3 × 3) slab models of Cu(100), Cu(110), Cu(111) and Cu(211)[19] with the (100), (110) and (111) being the dominant surfaces of copper. The Cu (211) facet was considered because of its good selectivity towards C1 formation. This was linked to the Cu (211) morphology characterized by step-edge sites with a coordination number equal to 7 (CN7).[46] Here, we have compared the catalytic conversion of $CO_2$ to C1 chemicals on Cu(211) to that on 55-atoms icosahedral Cu-M nanoclusters with M located at CN6 and CN8.

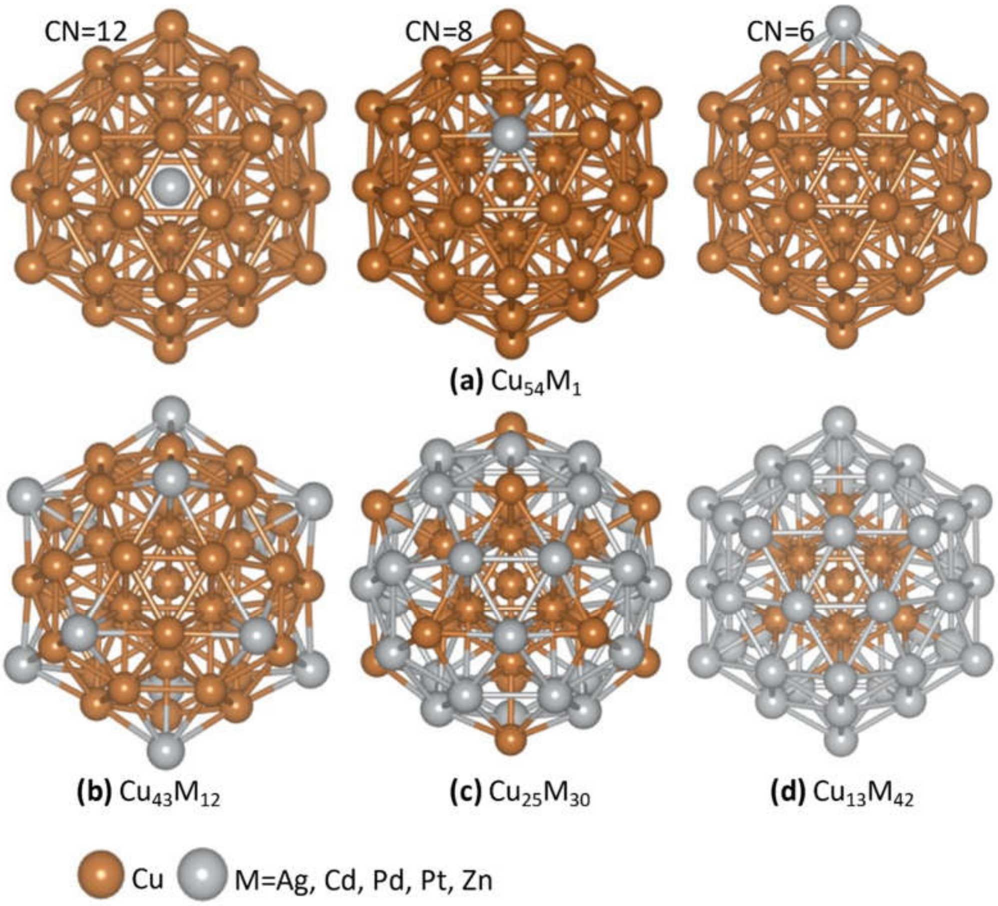

**Figure 1.** **(a)** 55-atom Cu-based clusters doped with one metal atom (M) at three different coordination sites: CN = 6, 8 and 12. **(b)** The 55-atom Cu-based cluster doped with 12 metal atoms located at CN = 6. **(c)** The 55-atom Cu-based cluster doped with 30 metal atoms at CN = 8. **(d)** The core(Cu)-shell(M) model.

### 2.2. Density functional theory calculations

Calculations of energies and structures were conducted at the spin-polarized DFT level using the "Vienna *ab initio* simulation package" (VASP, version 6.3.1)[47] using the following computational settings: the Perdew–Burke–Ernzerhof (PBE) exchange correlation functional with the Grimme's-D3 dispersion correction; a plane-wave basis set within the framework of the projector augmented wave method with a kinetic energy cutoff ($E_{cut}$) set to 400 eV; a single *k*-point (1×1×1) for the nanoclusters and a (5×5×1) *k*-point mesh for the surface model to sample the Brillouin zone of the simulation supercell; a 0.18 eV width of the smearing. ) Energies, zero-point energies, and entropies of $H_2(g)$, $CO_2(g)$ and CO(g), and $H_2O$ used to compute the free energy corrections are reported in Supplementary Information **(Table S1)**.

### 2.3. Free energy calculations

The Gibbs free energy of each step involved in the $eCO_2RR$ to C1 products was computed using the following equation:

$$\Delta G = \Delta S + \Delta E_{\mathrm{ZPE}} - T\Delta S + \Delta G_{\mathrm{solv}} + \Delta G_{\mathrm{U}} \qquad (1)$$

where $\Delta E$ is the reaction energy; $\Delta E_{ZPE}$ is the change in zero-point energy; $\Delta S$ is the change in entropy and $T$ is the thermodynamic temperature of the reaction (300 K). We determined the latter two quantities within the harmonic approximation by taking the vibrational frequencies of adsorbates and molecules calculated with DFT. The solvation effects to compute the solvation free energy term $\Delta G_{solv}$ were included using VASPsol.[48] $\Delta G_U$ is the free energy correction introduced by the difference of the electrode potential. For reactions involving a concerted proton–electron transfer (CPET) step, the $\Delta G_U$ term can be computed using the computational hydrogen electrode (CHE) method proposed by Nørskov and co-workers by applying the formula:

$$\Delta G_{\mathrm{U}} = -neU \tag{2}$$

where $n$ is the number of electrons transferred; $e$ is the electron charge and $U$ is the applied electrode potential. The limiting potential ($U_L$) and the overpotential ($\eta$) are important factors for evaluating the catalytic activity. The limiting potential is given by the formula:

$$U_{\mathrm{L}} = -\,\Delta G_{\max}/ne \tag{3}$$

where $\Delta G_{\max}$ is the relative change of the Gibbs free energy of the rate-determining step. The overpotential can be obtained by calculating the difference between the equilibrium potential ($U_{eq}$) and the limiting potential:

$$\eta = U_{\mathrm{eq}} - U_{\mathrm{L}} \tag{4}$$

Thus, the overpotential is the minimum applied potential required to facilitate the formation of relevant intermediates.

## 3. Results and discussion

### 3.1. Stability, Structure, and Electronic Properties of the Icosahedral 55-atom Cu-M clusters

The segregation energy (SE) was used to determine the preference of the metal dopants (Ag, Cd, Pd, Pt and Zn) preference to be in the core or shell of $Cu_{54}M$. The SE is defined as

$$SE = E[\mathrm{Cu}_{54}\mathrm{M(surface)}] - E[\mathrm{Cu}_{54}\mathrm{M(core)}] \tag{5}$$

where $E[Cu_{54}M(surface)]$ and $E[Cu_{54}M(core)]$ are the electronic energies of the fully optimized $Cu_{54}M_1$ cluster obtained by replacing one Cu atom with a dopant metal at a surface (CN6 or CN8) and at the center of the cluster (CN12), respectively. In **Figure 2**, the SE values are negative for all $Cu_{54}M$, which implies that the metal prefers to be at the surface of the cluster, consistent with DFT calculations of $Cu_{54}Zr$.[49] Also, the metal doping at the CN8 site are more stable than CN6 but because of the relatively small difference in their SE, the adsorption and subsequent reduction of $CO_2$ were investigated on both coordination sites.

To gain insights into the relative stability of pure and bimetallic 55-atom systems, we used the binding energy per atom ($E_B$), defined as:[50]

$$E_B = \frac{E(\mathrm{Cu}_{55-x}\mathrm{M}_x) - (55-x)E(\mathrm{Cu}) - xE(\mathrm{M})}{55} \tag{4}$$

where $E(Cu_{55\text{-}x}M_n)$ is the total energy of the most stable isomer of each $Cu_{55\text{-}x}M_x$ cluster and $E$(Cu) and $E$(M) are the total energies of Cu and Sn atoms, respectively. A higher negative value of $E_B$ indicates higher thermodynamic stability of the cluster. The calculated $E_B$ for pure $Cu_{55}$ nanocluster is –2.99 eV, equal to the value obtained using all-electron triple-z quality DFT calculations.[51] **Table 1** reports the calculated $E_B$ and other structural and electronic properties: the average interatomic bonding distance between nearest neighbors, the energy difference between the highest occupied molecular orbital (HOMO), the lowest unoccupied molecular orbital (LUMO) ($\Delta_{H\text{-}L}$) and the Bader charge difference between the Cu and M atoms ($\Delta Q_M$).

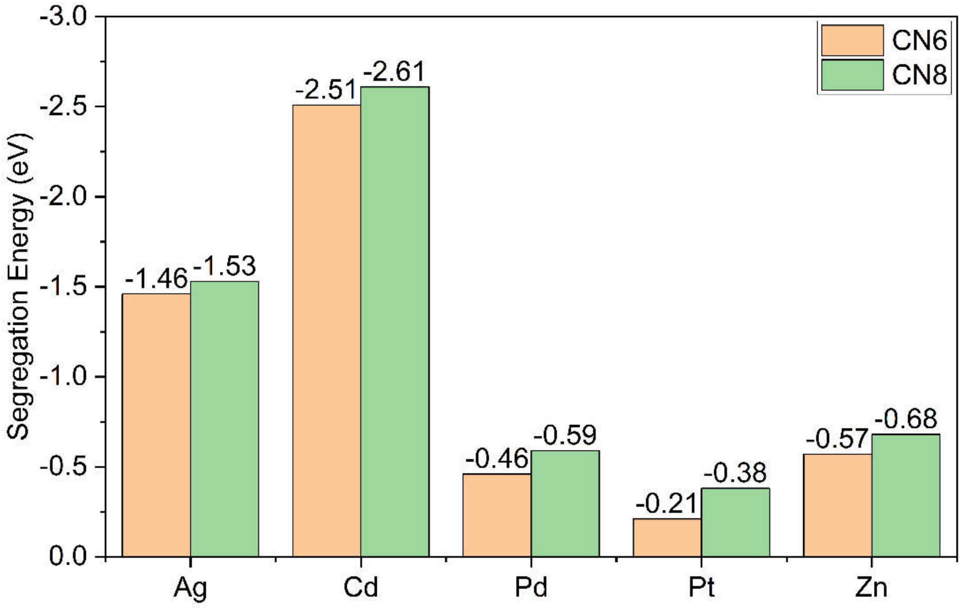

**Figure 2.** The segregation energy of the metal dopants Ag, Cd, Pd, Pt, and Zn in $Cu_{54}M$ clusters. Metal located at two different coordination sites: CN6 and CN8.

A descriptor to analyze the global reactivity descriptor, the gap energy $\Delta_{H\text{-}L}$, relates to the energy cost for an electron to jump from the HOMO to the LUMO orbital, therefore, characterizes the chemical stability of the system, with a higher value of $\Delta_{H\text{-}L}$ corresponding to a more chemically stable (less reactive) cluster. The $\Delta_{H\text{-}L}$ for pure $Cu_{55}$ atom is 0.028 eV, consistent with literature value of 0.03 eV.[52] In **Figure S1 (b)** and **Table 1**, in the case of single atom doping both $Cu_{54}Ag$ (CN6) and $Cu_{54}Zn$ (CN6) show very small $\Delta_{H\text{-}L}$ values of $1 \times 10^{-4}$ and $5 \times 10^{-4}$ eV, respectively. The single atom doped $Cu_{54}Ag$ (CN8) and $Cu_{54}Zn$ (CN8) show large $\Delta_{H\text{-}L}$ values of 0.049 and 0.0414 eV. This shows that the coordination environment of the metal dopant affects the $\Delta_{H\text{-}L}$ and therefore the reactivity of the cluster. Overall, the $\Delta_{H\text{-}L}$ value is in the range of 0.0001 - 0.17 eV. The highest value of $\Delta_{H\text{-}L}$, 0.17 eV, is found for $Cu_{43}Zn_{12}$.

The charge distribution in Cu-M clusters depends on the doping metal and will influence the $CO_2$ adsorption and subsequent $CO_2$ reduction because the electron transfer occurs from the electron-rich metal to the C atom, which is in the highest oxidation state in $CO_2$. In the decorated clusters ($Cu_{54}M$, $Cu_{43}M_{12}$, and $Cu_{25}M_{30}$), when M is Ag, Pd or Pt charge is transferred from Cu to M (negative $\Delta Q_M$), and when M is Cd or Zn charge is transferred from M to Cu (positive $\Delta Q_M$). In the core@shell $Cu_{13}M_{42}$ architecture, when M = Ag, Pd and Pt, the core is positively charged because of the charge transfer from Cu to M, while the shell has a negative charge. *Vice versa* for $Cu_{13}M_{42}$ with M = Cd and Zn. The effect of atomic radii, covalent radii, van-der radii, and electronegativity difference ($\Delta E_N$) on bond lengths and surface area are discussed and available in Supplementary Information (**Table S2**).

**Table 1.** The bond lengths (Å), formation energy (eV), HOMO-LUMO ($\Delta_{H\text{-}L}$) gap (eV) and Bader charges ($\Delta Q_M$, Coulomb) of the Cu-M (M = Ag, Cd, Pd, Pt and Zn) nanoclusters.

| | **Bond length** | | **Formation energy** | $\Delta_{H\text{-}L}$ | $\Delta Q_M$ |
|---|---|---|---|---|---|
| **Pristine $Cu_{55}$ Nanocluster** | | | | | |
| $Cu_{55}$ | 2.51 | | -2.99 | — | — |
| **1-atom doping on CN6** | | | | | |
| $Cu_{54}Ag_1$ | 2.69 | | -3.51 | 0.0001 | -0.12 |
| $Cu_{54}Cd_1$ | 2.73 | | -3.48 | 0.0412 | 0.16 |
| $Cu_{54}Pd_1$ | 2.59 | | -3.53 | 0.1013 | -0.37 |
| $Cu_{54}Pt_1$ | 2.56 | | -3.56 | 0.0441 | -0.64 |
| $Cu_{54}Zn_1$ | 2.54 | | -3.48 | 0.0005 | 0.13 |
| **1-atom doping on CN8** | | | | | |
| $Cu_{54}Ag_1$ | 2.69 | | -3.52 | 0.0488 | -0.08 |
| $Cu_{54}Cd_1$ | 2.73 | | -3.49 | 0.0349 | 0.14 |
| $Cu_{54}Pd_1$ | 2.59 | | -3.54 | 0.0431 | -0.30 |
| $Cu_{54}Pt_1$ | 2.56 | | -3.57 | 0.0481 | -0.63 |
| $Cu_{54}Zn_1$ | 2.54 | | -3.49 | 0.0414 | 0.17 |
| **12-atom doping on CN6** | | | | | |
| $Cu_{43}Ag_{12}$ | 2.67 | | -3.30 | 0.0858 | -0.12 |
| $Cu_{43}Cd_{12}$ | 2.75 | | -2.90 | 0.0104 | 0.14 |
| $Cu_{43}Pd_{12}$ | 2.59 | | -3.59 | 0.0682 | -0.32 |
| $Cu_{43}Pt_{12}$ | 2.56 | | -3.96 | 0.0824 | -0.58 |
| $Cu_{43}Zn_{12}$ | 2.54 | | -2.98 | 0.1721 | 0.09 |
| **30-atom doping on CN8** | | | | | |
| | **Cu-M** | **M-M** | | | |
| $Cu_{25}Ag_{30}$ | 2.65 | 2.81 | -2.93 | 0.0305 | -0.06 |
| $Cu_{25}Cd_{30}$ | 2.67 | 3.01 | -1.95 | 0.0016 | 0.08 |
| $Cu_{25}Pd_{30}$ | 2.59 | 2.70 | -3.49 | 0.0568 | -0.15 |
| $Cu_{25}Pt_{30}$ | 2.59 | 2.69 | -4.45 | 0.0524 | -0.26 |
| $Cu_{25}Zn_{30}$ | 2.53 | 2.75 | -2.12 | 0.0980 | 0.09 |
| **Core@shell** | | | | | |
| $Cu_{13}Ag_{42}$ | 2.81 | | -2.81 | 0.0835 | -0.14 |
| $Cu_{13}Cd_{42}$ | 2.95 | | -1.31 | 0.0131 | -0.93 |
| $Cu_{13}Pd_{42}$ | 2.68 | | -3.40 | 0.0168 | 0.78 |
| $Cu_{13}Pt_{42}$ | 2.62 | | -4.72 | 0.0527 | 0.69 |
| $Cu_{13}Zn_{42}$ | 2.56 | | -1.53 | 0.0173 | -0.93 |

### *3.2. Adsorption and activation of $CO_2$ on Cu and Cu-M clusters*

$CO_2$ is a linear molecule with two equivalent C–O bonds (length = 1.12 Å).[12] Before its dissociation, the first step in the catalytic conversion of $CO_2$ is its adsorption on the catalyst surface. $CO_2$ can maintain the geometric properties of gas-phase $CO_2$ (physisorption) or become activated because of the charge transferred from the metal catalyst to the $\pi^*$ molecular orbitals of the $CO_2$ molecule (chemisorption) resulting in the elongation of the C–O bonds and decrease in the O–C–O bond angle (linear to bent mode).[53] Here, we have conducted a detailed characterization of the adsorption and activation of $CO_2$ on the pure copper cluster $Cu_{55}$ and the copper-metal clusters, $Cu_{54}M$ (CN6 and CN8) , $Cu_{43}M_{12}$ (CN6), $Cu_{25}M_{30}$ (CN8) and $Cu_{13}M_{42}$ (core@shell), with M = Ag, Cd, Pd, Pt and Zn. These models can provide insights into the influence of surface chemistry on the activation of the $CO_2$ molecule. The structures of $CO_2$ on the Cu-M clusters are shown in **Figure 3**, and the associated adsorption energies ($E_{ads}$), bond angles, bond elongations and Bader

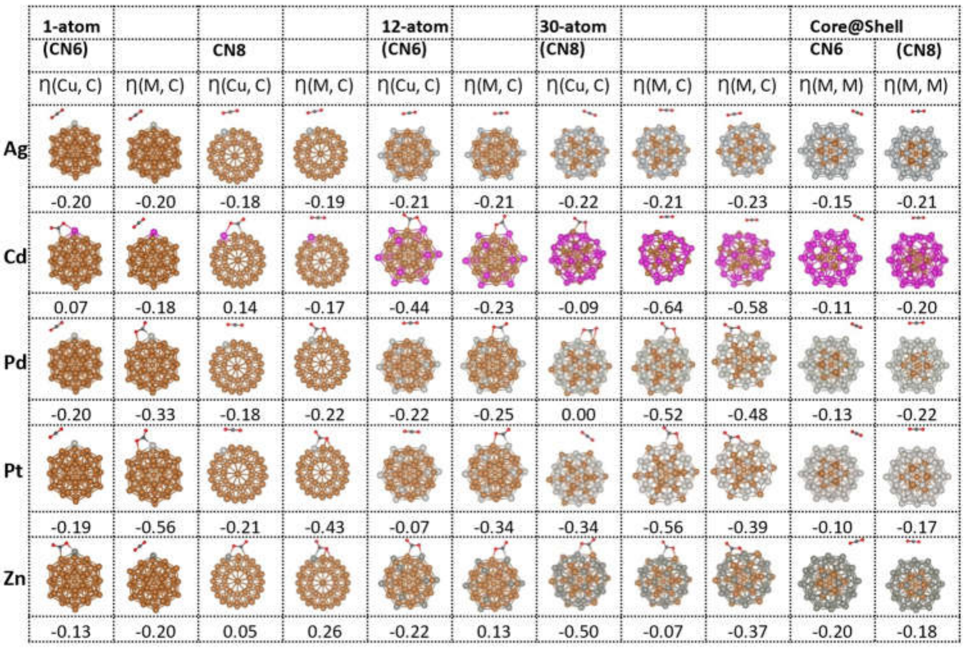

**Figure 3.** The structure and adsorption energies (eV) of $CO_2$ on the CuM clusters.

charges of $CO_2$ adsorbed on the Cu-M clusters are listed in **Table 2**. The values of $E_{ads}$ were calculated as

$$E_{ads} = E_{CuM-CO_2} - E_{CuM} - E_{CO_2} \tag{4}$$

where the first term is the total energy of the CuM-$CO_2$ system, and the second and third terms are the energies of the isolated cluster and $CO_2$ molecules, respectively. $CO_2$ is physisorbed on all Cu-Ag and core@shell clusters as indicated by the no significant deviations of the bond angle, bond elongation of adsorbed $CO_2$ from the gas-phase values, and small charge transfer between Cu and M ($\Delta Q_M$ ~0.04e). In **Figure 3** and **Table 2**, η(Cu, C) and η(M, C) refer to configurations in which the C atom of the $CO_2$ molecule is coordinated to the Cu and M atoms, respectively. In each chemisorbed state, there is a decrease in the O–C–O angle and an increase in charge transfer. In the single metal-doped systems, $Cu_{54}M$, at the CN6 active site, the coordination state η(Cu, C) occurs for M = Cd and Zn and η(M, C) occurs for M = Pd and Pt. In single metal-doped clusters at CN8, the η(Cu, C) exists for M = Cd and η(M, C) is present for M = Pd and Pt. Both η(Cu, C) and η(Zn, C) exist for $Cu_{54}Zn$ on the CN8 active site. In the 12-atom doped $Cu_{43}M_{12}$ clusters, η(Cu, C) is present for M = Cd, Zn and η(M, C) exists in all systems except for $Cu_{43}Ag_{12}$. The 30-atom doped nano catalysts show the same trend as the 12-atom, except for the absence of η(Cd, C) in $Cu_{43}Cd_{12}$. The η(Cu, C) and η(M, C) coordination do not exist in the core@shell models because $CO_2$ only physisorbs. In terms of adsorption energy on any catalyst surface, in the absence of η(M, C), the physisorption energy of $CO_2$ always dominates. Similarly, in the absence of η(Cu, C), the chemisorption energy of η(M, C) configuration always dominates. When both η(Cu, C) and η(M, C) occur on a particular site, then again the η(Cu, C) coordination mode is the most stable coordination mode.

**Table 2.** The adsorption energies ($E_{ads}$, eV), bond angles ($\theta_{OCO}$, °), charge difference ($\Delta Q_M$, Coulomb) bond elongations ($\Delta l_{CO}$, Å) and d-bands center ($\delta_d$, eV) of $CO_2$ adsorbed on the Cu-M nanoclusters (M = Ag, Cd, Pd, Pt and Zn). η(Cu, C) and η(M, C) refer to configurations in which the C atom of the adsorbed $CO_2$ molecule is coordinated to the Cu and M atoms, respectively.

| | $E_{ads}$ | | $\theta$(O-C-O) | | Charge difference | | $\Delta l_{CO}$ | $\delta_d$ |
|---|---|---|---|---|---|---|---|---|
| | η(Cu,C) | η(M,C) | η(Cu,C) | η(M,C) | η(Cu,C) | η(M,C) | | |
| $Cu_{55}$ | -0.01 | — | 33.40 | — | — | — | 0.05 | -2.27 |
| **1-atom doping (CN6)** | | | | | | | | |
| $Cu_{54}Ag_1$ | -0.20 | -0.20 | 0.340 | 0.460 | 0.04 | 0.04 | 0.00 | -2.28 |
| $Cu_{54}Cd_1$ | 0.07 | -0.18 | 43.84 | 0.250 | 0.61 | 0.04 | 0.09 | -2.38 |
| $Cu_{54}Pd_1$ | -0.20 | -0.33 | 0.710 | 40.12 | 0.04 | 0.51 | 0.17 | -2.29 |
| $Cu_{54}Pt_1$ | -0.19 | -0.56 | 0.750 | 44.67 | 0.04 | 0.57 | 0.21 | -2.29 |
| $Cu_{54}Zn_1$ | -0.13 | -0.20 | 47.45 | 0.300 | 0.70 | 0.04 | 0.23 | -2.36 |
| **1-atom doping (CN8)** | | | | | | | | |
| $Cu_{54}Ag_1$ | -0.18 | -0.19 | 0.65 | 0.42 | 0.04 | 0.04 | 0.00 | -2.28 |
| $Cu_{54}Cd_1$ | 0.14 | -0.17 | 41.3 | 0.41 | 0.58 | 0.05 | 0.15 | -2.34 |
| $Cu_{54}Pd_1$ | -0.18 | -0.22 | 0.72 | 45.52 | 0.05 | 0.63 | 0.17 | -2.28 |
| $Cu_{54}Pt_1$ | -0.21 | -0.43 | 1.28 | 50.97 | 0.63 | 0.71 | 0.24 | -2.26 |
| $Cu_{54}Zn_1$ | 0.05 | 0.26 | 48.8 | 52.21 | 0.76 | 0.86 | 0.27 | -2.34 |
| **12-atom doping (CN6)** | | | | | | | | |
| $Cu_{43}Ag_{12}$ | -0.21 | -0.21 | 0.660 | 0.300 | 0.04 | 0.04 | 0.01 | -2.67 |
| $Cu_{43}Cd_{12}$ | -0.44 | -0.23 | 48.50 | 45.60 | 0.75 | 0.68 | 0.23 | -4.03 |
| $Cu_{43}Pd_{12}$ | -0.22 | -0.25 | 0.470 | 38.02 | 0.04 | 0.49 | 0.19 | -2.12 |
| $Cu_{43}Pt_{12}$ | -0.07 | -0.34 | 1.260 | 42.38 | 0.78 | 0.53 | 0.29 | -2.05 |
| $Cu_{43}Zn_{12}$ | -0.22 | 0.13 | 49.22 | 49.30 | 0.75 | 0.77 | 0.27 | -3.72 |
| **30-atom doping (CN8)** | | | | | | | | |
| $Cu_{25}Ag_{30}$ | -0.22 | -0.23 | 0.490 | 0.620 | 0.04 | 0.04 | 0.00 | -3.12 |
| $Cu_{25}Cd_{30}$ | -0.09 | -0.64 | 32.19 | 0.240 | 0.65 | 0.05 | 0.27 | -5.27 |
| $Cu_{25}Pd_{30}$ | 0.00 | -0.52 | 35.30 | 42.33 | 0.38 | 0.48 | 0.25 | -1.49 |
| $Cu_{25}Pt_{30}$ | -0.34 | -0.56 | 1.070 | 44.72 | 0.02 | 0.49 | 0.29 | -1.75 |
| $Cu_{25}Zn_{30}$ | -0.50 | -0.37 | 49.68 | 50.85 | 0.75 | 0.82 | 0.23 | -4.61 |
| **42-atom doping (core@shell)** | | | | | | | | |
| $Cu_{13}Ag_{42}$ | -0.15 | -0.21 | 0.37 | 0.34 | 0.03 | 0.04 | 0.00 | -3.56 |
| $Cu_{13}Cd_{42}$ | -0.11 | -0.20 | 0.75 | 0.46 | 0.04 | 0.06 | 0.00 | -7.29 |
| $Cu_{13}Pd_{42}$ | -0.13 | -0.22 | 1.96 | 2.04 | 0.04 | 0.04 | 0.00 | -1.58 |
| $Cu_{13}Pt_{42}$ | -0.10 | -0.17 | 0.82 | 1.09 | 0.02 | 0.03 | 0.00 | -1.92 |
| $Cu_{13}Zn_{42}$ | -0.20 | -0.18 | 0.10 | 0.41 | 0.02 | 0.04 | 0.00 | -6.23 |

### *3.3. Mechanism of $CO_2$ reduction reaction to C1 products on Cu-M clusters and Cu surfaces*

In this section, we present calculations of the mechanism of electrochemical $CO_2$ reduction. **Scheme 1** shows the pathways and intermediates for the formation of the C1 products CO, HCOOH, $CH_2O$, $CH_4$ and $CH_3OH$. Depending on the atom coordinated to the catalyst, O or C, the first CPET step leads to two intermediates, OCHO* and COOH*. The second CPET will determine whether the $2e^-$ products HCOOH or CO is formed. Subsequent CPET will lead to $4e^-$ ($CH_2O$), $6e^-$ ($CH_3OH$) and $8e^-$ ($CH_4$) C1 products. Compared to other catalytic reactions, the pathway of the $eCO_2RR$ is more complex because of the number of intermediates involved. According to Eq. 1, the optimal reaction pathway is determined by the lowest free energy pathway at the applied potential *U*.

### 3.3.1. Electrocatalytic $CO_2$ conversion to CO and HCOOH

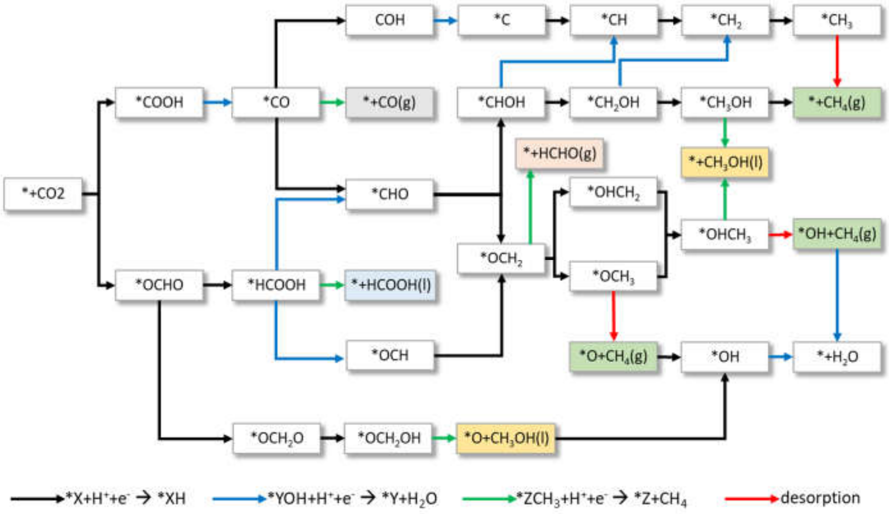

**Scheme 1.** Reaction pathways to C1 products: CO, HCOOH, $CH_2O$, $CH_4$ and $CH_3OH$.

We computed the free energy of reactions ($\Delta G$) of the elementary steps to the $CO_2$ conversion to HCOOH and CO on the following systems: icosahedral $Cu_{55}$ cluster; decorated and core-shell Cu-M bimetallic clusters; Cu(100), Cu(110), Cu(111) and Cu(211) surfaces. In the context of the CHE model (see Eq. 1), we define the potential limiting step ($\Delta G_{PLS}$) as the elementary reaction in the $eCO_2RR$ to CO or HCOOH (at $U = 0$ V) with the highest $\Delta G$ value. A high $\Delta G_{PLS}$ corresponds to poor catalytic performance. The elementary steps leading to the formation of CO are: (i) $CO_2$ adsorption ($CO_2 \rightarrow *CO_2$, $\Delta G_{*CO2}$); (ii) CPET to convert $CO_2*$ to C-coordinated formate ($*CO_2 + H^+ + e^- \rightarrow *COOH$, $\Delta G_{*COOH}$); (iii) CPET to convert formate to adsorbed carbon monoxide ($*COOH + H^+ + e^- \rightarrow CO(g) + H_2O$, $\Delta G_{*CO}$); (iv) the release, from the catalyst surface, of gas-phase CO ($*CO \rightarrow CO$, $\Delta G_{CO}$). The structures of the optimized *COOH and *CO on all Cu and CuM systems are reported in Supplementary Information (**Figures S2-S8**).

**Figure 4(a)** compares the Gibbs free energy diagrams for the $CO_2$-to-CO conversion on the monometallic 55-atom cluster and the (100), (110), (111) and (211) surfaces, where there is significant dependence of the *COOH and *CO intermediates' stability on the surface morphology and coordination environment. The (211) facet has better $eCO_2RR$ catalytic performance (lower $\Delta G_{PLS}$) toward CO formation than any other surfaces but higher than $Cu_{55}$, which was then taken as the reference system to assess the other CuM cluster. The competitive HER ($H^+ + e^- \rightarrow ½ H_2$) in **Figure 4(b)** shows a similar morphology dependence: unfavourable on the (110) surface; highly favorable on the (100); moderately favorable on the (211) and $Cu_{55}$. The free energy diagrams for the $eCO_2RR$ to CO and the HER on bimetallic clusters are reported in **Figure 5**. In the single metal doped clusters, $Cu_{54}M$, the value of $\Delta G_{PLS}$ depends on both the coordination site and nature of the metal. The $\Delta G_{PLS}$ is lower when the reaction occurs on CN6 for M equal to Cd (0.16), Pd (0.23), and Pt (0.53 eV) compared to CN8, Cd (0.12 eV), Pd (0.42 eV), Pt (0.78 eV). However, for Ag (0.27 eV) and Zn (0.18 eV), CN6 shows higher $\Delta G_{PLS}$ than CN8, Ag (0.14 eV) and Zn (0.14 eV). Each intermediate shows strong chemisorption with a low $\Delta_{GPLS}$ value and *vice versa*. For both CN6 and CN8 systems, HER is dominant (lower $\Delta G_H$) over $eCO_2RR$ because of the strong CO binding to the cluster, leading to a large $\Delta G_{*CO}$; the exception is M = Pt. When the number of metal dopants on the Cu-M cluster increases, $Cu_{43}M_{12}$, so does the $\Delta G_{PLS}$ value: Ag (0.24 eV), Pd (0.32 eV), Pt (0.86 eV) and Zn (0.19 eV). The exception is Cd (0.25 eV). The CO generation remains dominant over HER, except again for Pt, for the same reasons discussed for single atom doped clusters. With further increase in the doping and change in surface chemistry in the $Cu_{25}M_{30}$ clusters, the HER becomes more favorable with a small value of $|\Delta G_H|$ for Ag (0.10 eV), Cd (0.19 eV), Pd (0.92 eV) and Pt

(0.76 eV) compared to the $\Delta G_{PLS}$ of the $eCO_2RR$ of Ag (0.37 eV), Cd (0.29 eV), Pd (1.61 eV), and Pt (1.23 eV). At this doping concentration, only Zn, with $\Delta G_{PLS}$ = 0.40 eV and $\Delta G_H$ = 0.49 eV, favors $eCO_2RR$ over HER. All core@shell models are more active towards HER than $eCO_2RR$: $\Delta G_H$ of Ag (0.07 eV), Cd (0.45eV), Pd (–0.62 eV), Pt (-0.59 eV), and Zn(–0.27 eV) are lower tha $\Delta G_{PLS}$ of Ag (0.76 eV), Cd (0.91 eV), Pd (1.12 eV), Pt (1.09 eV) and Zn (0.58 eV).

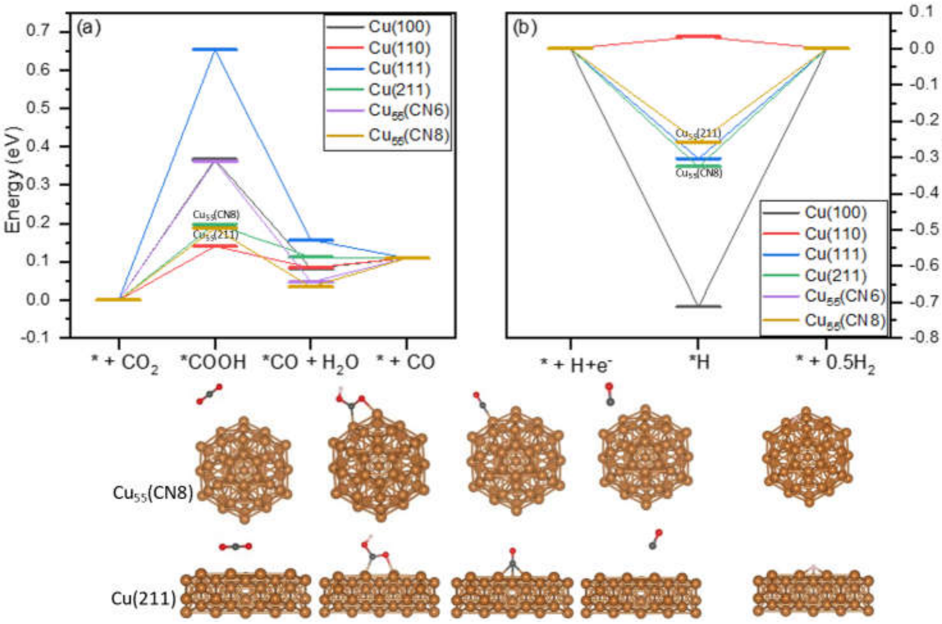

**Figure 4.** Gibbs free energy diagram for the $CO_2$ reduction pathways to CO **(a)** and hydrogen evolution reaction **(b)** on $Cu_{55}$ with coordination sites CN6 and CN8, and on the (100), (110) and (111) copper surfaces.

For HCOOH, the steps are the CPET to convert adsorbed $CO_2$* to O-coordinated formate ($*CO_2 + H^+ + e^- \rightarrow COOH*$, $\Delta G_{OCOH*}$) and the CPET to convert adsorbed formate to liquid phase formic acid ($OCHO* + H^+ + e^- \rightarrow HCOOH(l)$, $\Delta G_{HCOOH}$). In **Figure 5**, the $\Delta G_{PLS}$ value for HCOOH of $Cu_{54}M$ with CN6 for Ag (0.33 eV), Pd (0.33 eV), and Pt(0.37 eV) in the CuM cluster with CN8 for Ag(0.46 eV), Cd (0.46 eV), Pt(0.45 eV), $Cu_{43}M_{12}$ with Ag (0.39 eV), Pt (0.39 eV), $Cu_{25}M_{30}$ with Pd (0.19 eV), Pt (0.13 eV) and finally core-shell with Pd (0.33 eV), Pt (0.41 eV) are dominant over HER. We can explain this behaviour by considering the value of the d-band center (**Table 2**), which decreases for Ag, Cd and Zn with increasing doping concentration. The adsorption energy of the intermediates involved in the CO or HCOOH reaction pathway also decreases. Similarly, the higher position of the d-band center for Pd and Pt leads to an increase in the intermediate adsorption energy. Therefore, the core-shell model with low d-band center, Ag (–3.56 eV), Cd (–7.29 eV) and Zn(–6.23 eV), show poor catalytic performance, and Pd (–1.58 eV) and Pt (–1.92 eV) show good catalytic performance for HCOOH. Overall, the core@shell promotes the formation of HCOOH, and single metal-doped clusters show good catalytic performance for CO, except for Pt, which catalyzes HCOOH formation.

### 3.3.2. Electrocatalytic $CO_2$ conversion to $CH_2O$, $CH_3OH$, and $CH_4$

The free energy diagrams for the $eCO_2RR$ to formaldehyde ($CH_2O$), methanol ($CH_3OH$), and methane ($CH_4$) on the CuM clusters are reported in **Figure 6**. After the $eCO_2RR$ reduction to *CO or *HCOOH, further CPET steps generates three distinct intermediates: *CHO, *COH, or *OCH. Among these three intermediates, the *CHO is the easiest to generate, as illustrated by the free energy diagram for these species' formation, which shows the lowest $\Delta G_{PLS}$ values for COH. A subsequent CPET step leads to the formation of formaldehyde: $*CHO + H^+ + e^- \rightarrow *OCH_2 \rightarrow * + CH_2O(g)$. Due to the stronger O-affinity, $CH_2O$ prefers *OCHO than the *COOH route. $CH_2O$ generation shows lowest

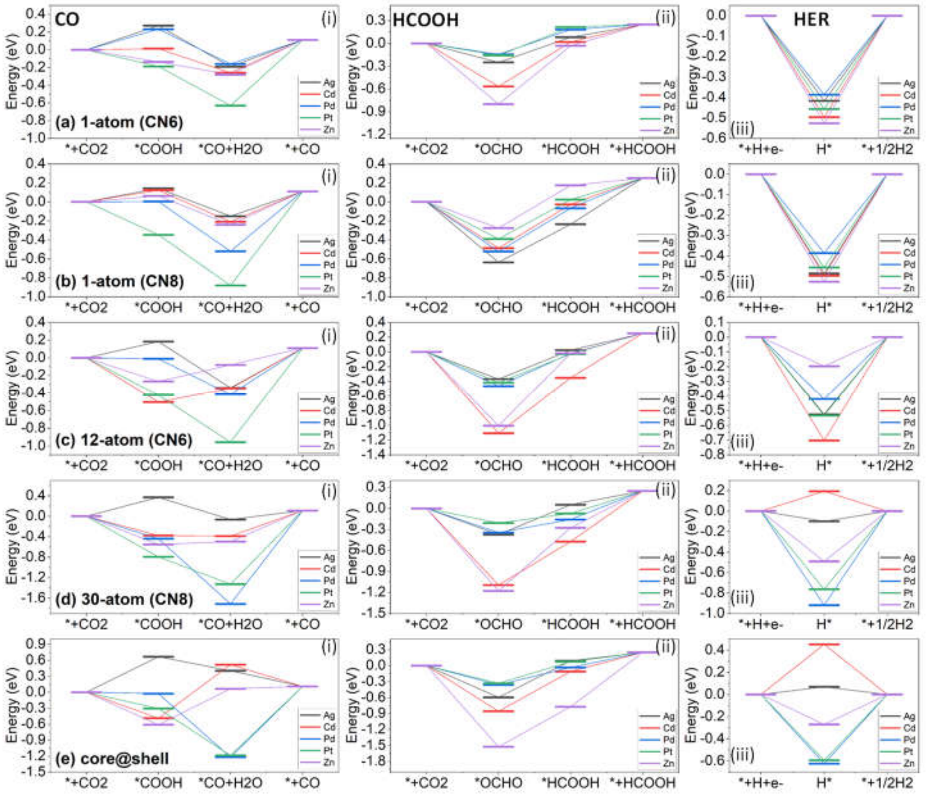

**Figure 5.** Gibbs free energy diagram for the (i) $CO_2$ reduction pathways to CO, (ii) $CO_2$ reduction reaction to HCOOH, and (iii) hydrogen evolution reaction (red line) on $Cu_{54}M_1$ with CN6 **(a)**, $Cu_{54}$ $M_1$ with CN8 **(b)**, $Cu_{43}M_{12}$ **(c)**, $Cu_{25}M_{30}$ **(d)**, and core@shell **(e)** with M = Ag, Cd , Pd, Pt, and Zn.

$\Delta G_{PLS}$ values on $Cu_{25}Pd_{30}$ (0.19 eV) and core-shell Cu@Pd (0.33 eV). As the $\Delta G_H$ values on $Cu_{25}Pd_{30}$ (0.92 eV) and core-shell Cu@Pd (0.62 eV) are higher than $\Delta G_{PLS}$ values, the $CO_2$ conversion to $CH_2O$ is dominant over HER on these clusters. CuPd is also favorable towards $CH_2O$ formation as the $\Delta G_{PLS}$ values are higher than $\Delta G_H$ on these clusters. The values of $\Delta G_{PLS}$ are 0.45 eV for $Cu_{54}Pt$ (CN8), 0.49 eV for $Cu_{25}Pt_{30}$, and 0.44 eV for the $Cu_{54}Pt$ (CN8) and the core@shell $Cu_{25}Pt_{30}$ clusters. In comparison, the $\Delta G_H$ values on $Cu_{54}Pt$ (CN8), $Cu_{25}Pt_{30}$ and Cu@Pt are 0.46 eV, 0.76 eV and 0.59 eV, respectively. The Gibbs free energy diagram of $eCO_2RR$ to $CH_2O$ on these systems is given as **Fig. 6(a)–(e)-(i)**.

The formation of $CH_3OH$ involves five CPET steps. The first three reduction steps coincide to the $eCO_2RR$ to $CH_2O$. The *CHO is reduced to *CHOH or *$OCH_2$ depending on if the O or C atoms ate protonated. This leads to four possible routes to convert $CO_2$ to $CH_3OH$: (i) *COOH→*CO→*CHO→*$OCH_2$→*$OCH_3$→*$OHCH_3$; (ii) ∗OCHO→∗$OCH_2O$→∗$OCH_2OH$→∗O+$CH_3OH$→∗OH→∗+$H_2O$; (iii) OCHO→ ∗HCOOH→∗CHO→∗CHOH→∗$CH_2OH$→∗$OHCH_3$; (iv) ∗OCHO→ ∗HCOOH→∗CHO→∗$OCH_2$→∗$OHCH_2$ → ∗ Out of these four paths, our calculations predict the last one is the most suitable for $CH_3OH$ formation. Just like $CH_2O$, the $Cu_{25}Pd_{30}$ and core-shell Cu@Pd show the lowest $\Delta G_{PLS}$ values, 0.28 eV and 0.33 eV, respectively, and still, these reactions are dominant over HER. The main 8-electron product of $eCO_2RR$ is $CH_4$, involving eight CPET transfer steps. It follows five different reaction pathways:

1. ∗CHO → ∗CHOH → ∗CH → ∗$CH_2$ → ∗$CH_3$ → ∗ + $CH_4$
2. ∗CHO → ∗CHOH → ∗$CH_2OH$ → ∗$CH_2$→ ∗$CH_3$ → ∗ + $CH_4$
3. ∗CHO → ∗$OCH_2$ → ∗$OHCH_2$ → ∗$OHCH_3$ → ∗OH + $CH_4$ → * + $H_2O$
4. ∗CHO → ∗$OCH_2$ → ∗$OCH_3$ → ∗$OHCH_3$ → ∗OH + $CH_4$ → ∗ + $H_2O$
5. ∗CHO → ∗$OCH_2$ → ∗$OCH_3$ → ∗O + $CH_4$ → ∗OH → ∗ + $H_2O$

The free energy diagrams along these pathways are given in **Figure S9** of Supplementary Information.

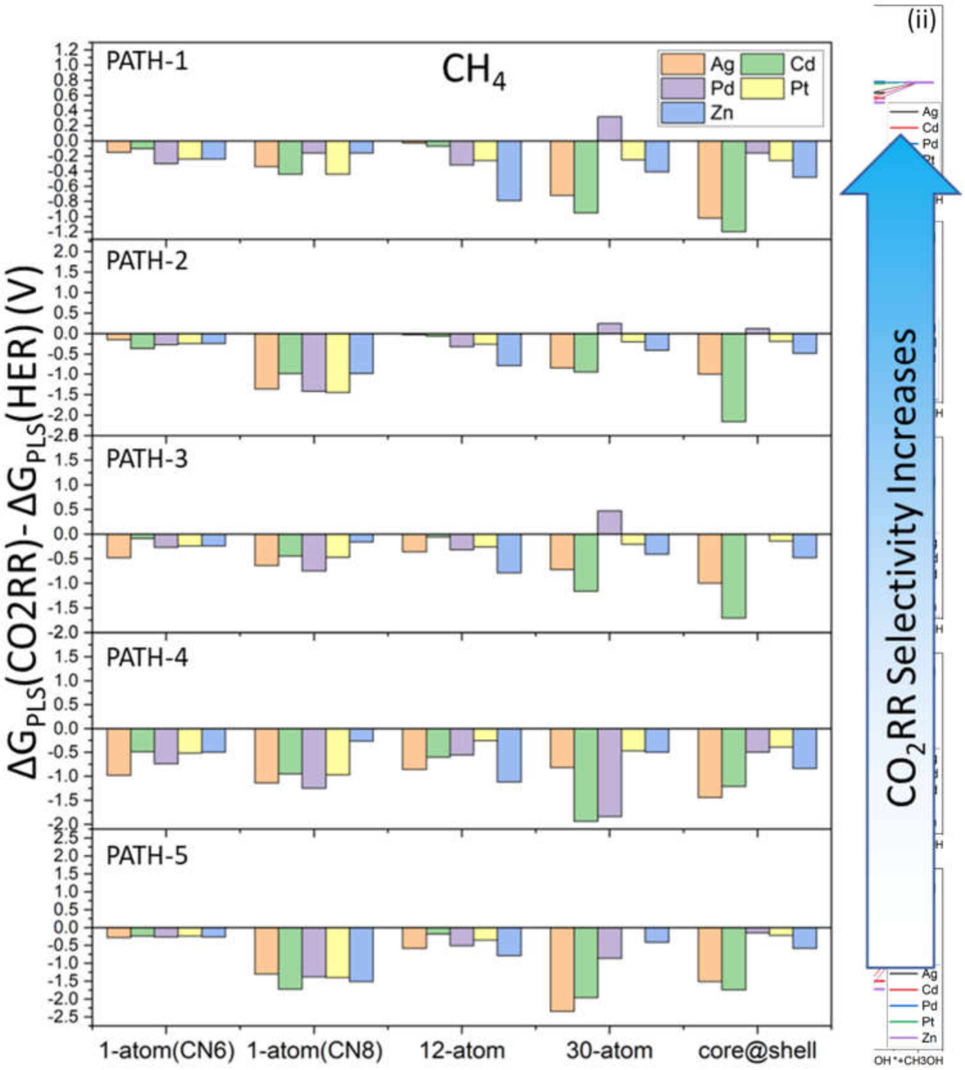

**Figure 7.** Limiting potential difference (*ΔΔG*$_{PLS}$) between $CO_2RR$ and HER.

$Cu_{43}M_{12}$ **(c)**, $Cu_{25}M_{30}$ **(d)**, and core@shell **(e)**.

HER is a competitive reaction in $eCO_2RR$ and can reduce the efficiency of the $eCO_2RR$ reaction leading to poor selectivity of the catalyst. To evaluate the selectivity of $eCO_2RR$ *vs* HE, we have reported in **Figure 8** the limiting potential difference $\Delta\Delta G_{PLS} = \Delta G_{PLS}(eCO_2RR) - \Delta G_H(HER)$ for the five reaction pathways leading to the formation of $CH_4$ on the CuM clusters. The higher the (positive) value of $\Delta\Delta G_{PLS}$, the higher the selectivity for $CH_4$. Only CuPd shows good catalytic performance towards $CH_4$ formation. Through the reaction pathway (1), $Cu_{25}Pd_{30}$ has positive $\Delta\Delta G_{PLS}$. The $Cu_{43}Ag_{12}$ and $Cu_{43}Cd_{12}$ show a small negative difference of $\Delta\Delta G_{PLS}$. Similarly, for pathway (2) and (3), the $Cu_{25}Pd_{30}$ and Cu@Pd show a positive $\Delta\Delta G_{PLS}$ value and hence these two systems are potential catalysts for $CH_4$ formation. Like pathway (1), the $Cu_{43}Ag_{12}$ and $Cu_{43}Cd_{12}$ show a very small $\Delta\Delta G_{PLS}$ for (2) which makes them also good candidates for catalyzing $CH_4$ formation. Finally, $Cu_{13}Cd_{42}$ shows a small value of $\Delta\Delta G_{PLS}$, which can be explained based on the d-band center and coordination environment: at the same doping concentration (1-atom) with CN6 and CN8, the 1-atom at CN6 show significantly low overpotential for all pathways leading to $CH_4$ generation. Single-doped clusters with CN6 and CN8 have similar d-band center values (**Table 2**), only the coordination environment is different, which means that the CN environment has a significant impact on catalytic performance. Furthermore, the d-band center value increases with an increase in doping concentration for

Cu-Pd and Cu-Pt catalysts. Consequently, there is strong adsorption of intermediates involved in the reaction (pathways 1 to 5). However, with M = Ag, Cd and Zn, the value of d-band centers decreases, which leads to weak adsorption of intermediates and poor catalytic performance towards $CH_4$ formation.

### 3.3.3. Selectivity

The overpotentials (η) to C1 products for all CuM systems, summarized in **Figure 8**, were computed from the equilibrium ($U_{eq}$) and limiting potentials (**Figures 5** and **6**). The UL values for CO, HCOOH, $CH_2O$, $CH_3OH$ and $CH_4$ are 0.12 V, 0.25 V, 0.07 V, 0.02 V and 0.17 V, respectively. For the copper clusters doped with Ag, Cd and Zn, an increase in metal doping, particularly after 30-atom, leads to the HER becoming dominant over other C1 products. This behaviour is clearly noticeable for the single atom doped clusters, $Cu_{54}M$ with M = Ag, Cd and Zn, which shows higher η values for HER than the corresponding core@shell systems. The η(V) values also show that a single atom doped system supports either CO or HCOOH. Therefore, small doping does not support the formation of $CH_3OH$ or $CH_4$. As metal doping increases, Cu-Pd and Cu-Pt show lower overpotential for $CH_2O$, $CH_3OH$ and $CH_4$. Only $Cu_{25}Pt_{30}$ and $Cu_{13}@Pd_{42}$ show lowest overpotential for methane.

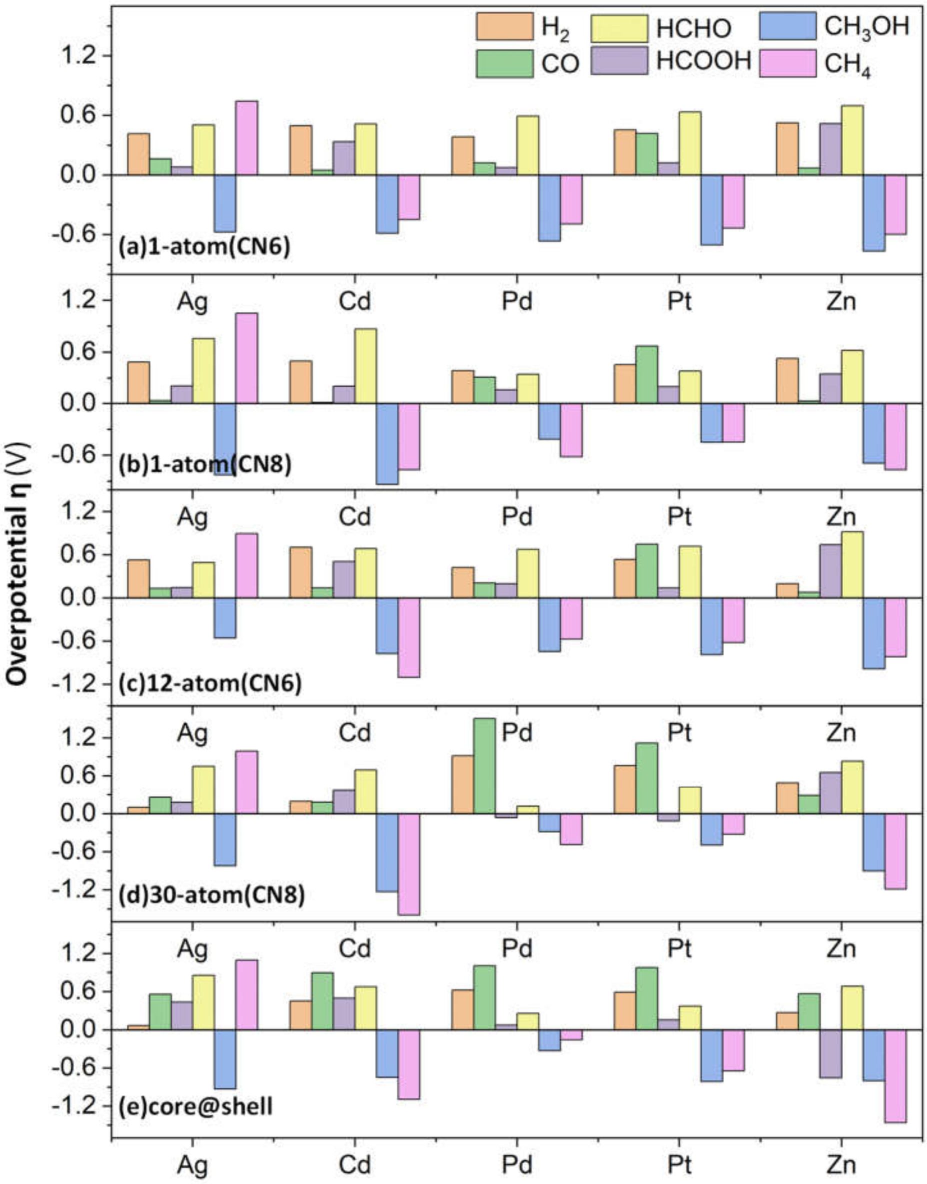

**Figure 8.** Overpotentials (η) for the electrocatalytic formation of $H_2$, CO, HCOOH, $CH_2O$, $CH_3OH$, and $CH_4$ on CuM clusters.

## 5. Conclusions

In this work, the catalytic properties towards the electrochemical $CO_2$ reduction reaction of a series of icosahedral 55-atom Cu-based clusters doped with Ag, Cd, Pd, Pt and Zn were investigated using density functional theory calculations. The adsorption and activation of $CO_2$ on these clusters and all possible reaction paths that lead to the $CO_2$ reduction to C1 products (CO, HCOOH, $CH_2O$, $CH_3OH$ and $CH_4$) were considered. Apart from the composition effects, the role of coordination environment of the metal dopant on the catalytic performance of copper-based cluster was also investigated, with the results showing that nanoclusters with eight-coordinated metal dopants have better catalytic activity towards $CO_2$ activation. Single-atom doping with Cd and Zn is the best candidate for the $CO_2$-to-CO conversion, while core-shell with Ag, Pd and Pt is a good choice for formic acid or formaldehyde formation. The Cu-Pt and Cu-Pd systems show the lowest overpotential for methane. This work identifies the influence of size, metal coupling, and metal coordination on $CO_2$ activation and intermediate stability and, consequently, the

doi:10.20944/preprints202211.0334.v1

structure-property relationship in Cu-based mono and bi-metallic clusters for the selective $CO_2$ conversion to value-added one-carbon products.

**Supplementary Materials:** See supplementary material for the following data: (i) Energies, zero-point energies, and entropies of $H_2$(g), $CO_2$(g) and CO(g), and $H_2O$. (ii) Stability analysis of Cu-M (M = Ag, Cd, Pd, Pt and Zn) nanoclusters. (iii) Coordination number analysis of Cu and Cu-M nanoclusters; (iv) Adsorption energies of $CO_2$, CO, and COOH on Cu and Cu-M nanoclusters, core-shell, models; (v) Bader charges on C and O, bond angle and bond lengths on surface models.

**Author Contributions:** Conceptualization of work: AGN and DDT; Conducting of experiments: AGN; Computation: AGN; Data analyses: AGN, AR, AH and DDT; Data dissemination & graphics: AGN, AH and DDT; Writing of manuscript: AGN, AR, GC, DDT; Project support: GC, DDT.

**Funding:** AGN acknowledges the Pakistan HEC-QMUL PhD Scholarships for funding. DDT and GAC acknowledged the ACT programme (Accelerating CCS Technologies, Horizon2020 Project No 299668), which funded the FUNMIN project. Financial contributions made from Department for Business, Energy & Industrial Strategy (BEIS) together with extra funding from NERC and EPSRC research councils, United Kingdom, ADEME (FR), MINECO-AEI (ES). We are grateful to the UK Materials and Molecular Modelling Hub for computational resources, which is partially funded by EPSRC (EP/P020194/1). We are grateful to the UK Materials and Molecular Modelling Hub for computational resources, which is partially funded by EPSRC (EP/P020194/1). Via our membership of the UK's HEC Materials Chemistry Consortium, which is funded by EPSRC (EP/L000202), this work used the ARCHER UK National Supercomputing Service (http://www.archer.ac.uk).

**Data Availability Statement:** The data presented in this study are available on request from the corresponding author.

**Acknowledgments:** This research utilized Queen Mary's Apocrita HPC facility, supported by QMUL Research-IT. http://doi.org/10.5281/zenodo.438045

**Conflicts of Interest:** The authors declare no conflict of interest.

## References

1 J. Shukla, P.R.; Skea, J.; Calvo Buendia, E.; Masson-Delmotte, V.; Pörtner, H.-O.; Roberts, D. C.; Zhai, P.; Slade, R.; Connors, S.; van Diemen, R.; Ferrat, M.; Haughey, E.; Luz, S.; Neogi, S.; Pathak, M.; Petzold, J.; Portugal Pereira, J.; Vyas, P.; Huntley, *IPCC, 2019: Climate Change and Land: an IPCC special report on climate change, desertification, land degradation, sustainable land management, food security, and greenhouse gas fluxes in terrestrial ecosystems*, 2019.

2 O. S. Bushuyev, P. De Luna, C. T. Dinh, L. Tao, G. Saur, J. van de Lagemaat, S. O. Kelley and E. H. Sargent, What Should We Make with CO2 and How Can We Make It?, *Joule*, 2018, **2**, 825–832.

3 W. Zhang, Y. Hu, L. Ma, G. Zhu, Y. Wang, X. Xue, R. Chen, S. Yang and Z. Jin, Progress and Perspective of Electrocatalytic CO2 Reduction for Renewable Carbonaceous Fuels and Chemicals, *Adv. Sci.*, 2018, **5**, 1700275.

4 A. Bagger, W. Ju, A. S. Varela, P. Strasser and J. Rossmeisl, Electrochemical CO2 Reduction: A Classification Problem, *ChemPhysChem*, 2017, **18**, 3266–3273.

5 A. A. Peterson and J. K. Nørskov, Activity descriptors for CO2 electroreduction to methane on transition-metal catalysts, *J. Phys. Chem. Lett.*, 2012, **3**, 251–258.

6 J. Wu, Y. Huang, W. Ye and Y. Li, CO2 Reduction: From the Electrochemical to Photochemical Approach, *Adv. Sci.*, 2017, **4**, 1–29.

7 Z. He, Q. Qian, J. Ma, Q. Meng, H. Zhou, J. Song, Z. Liu and B. Han, Water-Enhanced Synthesis of Higher Alcohols from CO2 Hydrogenation over a Pt/Co3O4 Catalyst under Milder Conditions, *Angew. Chemie Int. Ed.*, 2016, **55**, 737–741.

8 X. Zhang, X. Li, D. Zhang, N. Q. Su, W. Yang, H. O. Everitt and J. Liu, Product selectivity in plasmonic photocatalysis for carbon dioxide hydrogenation, *Nat. Commun.*, 2017, **8**, 14542.

9 S. Park, D. Bézier and M. Brookhart, An Efficient Iridium Catalyst for Reduction of Carbon Dioxide to Methane with Trialkylsilanes, *J. Am. Chem. Soc.*, 2012, **134**, 11404–11407.

10 A. Klinkova, P. De Luna, C.-T. Dinh, O. Voznyy, E. M. Larin, E. Kumacheva and E. H. Sargent, Rational Design of Efficient

---

Palladium Catalysts for Electroreduction of Carbon Dioxide to Formate, *ACS Catal.*, 2016, **6**, 8115–8120.

11 W. Zhu, R. Michalsky, Ö. Metin, H. Lv, S. Guo, C. J. Wright, X. Sun, A. A. Peterson and S. Sun, Monodisperse Au Nanoparticles for Selective Electrocatalytic Reduction of CO2 to CO, *J. Am. Chem. Soc.*, 2013, **135**, 16833–16836.

12 H. Xie, T. Wang, J. Liang, Q. Li and S. Sun, Cu-based nanocatalysts for electrochemical reduction of CO2, *Nano Today*, 2018, **21**, 41–54.

13 H. L. A. Dickinson and M. D. Symes, Recent progress in CO2 reduction using bimetallic electrodes containing copper, *Electrochem. commun.*, 2022, **135**, 107212.

14 J. R. Kitchin, J. K. Nørskov, M. A. Barteau and J. G. Chen, Role of Strain and Ligand Effects in the Modification of the Electronic and Chemical Properties of Bimetallic Surfaces, *Phys. Rev. Lett.*, 2004, **93**, 156801.

15 J. H. Sinfelt, J. L. Carter and D. J. C. Yates, Catalytic hydrogenolysis and dehydrogenation over copper-nickel alloys, *J. Catal.*, 1972, **24**, 283–296.

16 S. Shen, J. He, X. Peng, W. Xi, L. Zhang, D. Xi, L. Wang, X. Liu and J. Luo, Stepped surface-rich copper fiber felt as an efficient electrocatalyst for the CO2RR to formate, *J. Mater. Chem. A*, 2018, **6**, 18960–18966.

17 Y. Hori, I. Takahashi, O. Koga and N. Hoshi, Selective formation of C2 compounds from electrochemical reduction of CO2 at a series of copper single crystal electrodes, *J. Phys. Chem. B*, 2002, **106**, 15–17.

18 S. P. and S. K. Mandal, From CO2activation to catalytic reduction: A metal-free approach, *Chem. Sci.*, 2020, **11**, 10571–10593.

19 M. D. Higham, M. D. Higham, M. G. Quesne, M. G. Quesne, C. R. A. Catlow, C. R. A. Catlow and C. R. A. Catlow, Mechanism of CO2conversion to methanol over Cu(110) and Cu(100) surfaces, *Dalt. Trans.*, 2020, **49**, 8478–8497.

20 F. Studt, M. Behrens, E. L. Kunkes, N. Thomas, S. Zander, A. Tarasov, J. Schumann, E. Frei, J. B. Varley, F. Abild-Pedersen, J. K. Nørskov and R. Schlögl, The Mechanism of CO and CO2 Hydrogenation to Methanol over Cu-Based Catalysts, *ChemCatChem*, 2015, **7**, 1105–1111.

21 J. L. C. Fajín, M. N. D. S. Cordeiro, F. Illas and J. R. B. Gomes, Influence of step sites in the molecular mechanism of the water gas shift reaction catalyzed by copper, *J. Catal.*, 2009, **268**, 131–141.

22 M. Behrens, F. Studt, I. Kasatkin, S. Kühl, M. Hävecker, F. Abild-pedersen, S. Zander, F. Girgsdies, P. Kurr, B. Kniep, M. Tovar, R. W. Fischer, J. K. Nørskov and R. Schlögl, Industrial Catalysts, 2012, **759**, 893–898.

23 Y. Hori, I. Takahashi, O. Koga and N. Hoshi, Electrochemical reduction of carbon dioxide at various series of copper single crystal electrodes, *J. Mol. Catal. A Chem.*, 2003, **199**, 39–47.

24 Q. Li, Y. Zhang, L. Shi, M. Wu, Y. Ouyang and J. Wang, Dynamic structure change of Cu nanoparticles on carbon supports for CO 2 electro-reduction toward multicarbon products , *InfoMat*, 2021, **3**, 1285–1294.

25 B. Steinhauer, M. R. Kasireddy, J. Radnik and A. Martin, Development of Ni-Pd bimetallic catalysts for the utilization of carbon dioxide and methane by dry reforming, *Appl. Catal. A Gen.*, 2009, **366**, 333–341.

26 X. Wang, Q. Chen, Y. Zhou, H. Li, J. Fu and M. Liu, Cu-based bimetallic catalysts for CO2 reduction reaction, *Adv. Sens. Energy Mater.*, 2022, **1**, 100023.

27 L. Zaza, K. Rossi and R. Buonsanti, Well-Defined Copper-Based Nanocatalysts for Selective Electrochemical Reduction of CO2to C2Products, *ACS Energy Lett.*, 2022, **7**, 1284–1291.

28 C. Chen, Y. Li, S. Yu, S. Louisia, J. Jin, M. Li, M. B. Ross and P. Yang, Cu-Ag Tandem Catalysts for High-Rate CO2 Electrolysis toward Multicarbons, *Joule*, 2020, **4**, 1688–1699.

29 A. Alvarez-Garcia, E. Flórez, A. Moreno and C. Jimenez-Orozco, CO2 activation on small Cu-Ni and Cu-Pd bimetallic clusters, *Mol. Catal.*, 2020, **484**, 110733.

30 M. Xing, L. Guo and Z. Hao, Theoretical insight into the electrocatalytic reduction of CO2 with different metal ratios and reaction mechanisms on palladium–copper alloys, *Dalt. Trans.*, 2019, **48**, 1504–1515.

31 L. Han, H. Liu, P. Cui, Z. Peng, S. Zhang and J. Yang, Alloy Cu3Pt nanoframes through the structure evolution in Cu-Pt nanoparticles with a core-shell construction, *Sci. Rep.*, 2014, **4**, 1–6.

32 H. S. Jeon, J. Timosnenko, F. Scholten, I. Sinev, A. Herzog, F. T. Haase and B. R. Cuenya, Operando insight into the correlation between the structure and composition of CuZn nanoparticles and their selectivity for the electrochemical CO2 reduction, *J. Am. Chem. Soc.*, 2019, **141**, 19879–19887.

33 X. Feng, K. Jiang, S. Fan and M. W. Kanan, Grain-Boundary-Dependent CO2 Electroreduction Activity, *J. Am. Chem. Soc.*, 2015, **137**, 4606–4609.

34 X. Jiang, N. Koizumi, X. Guo and C. Song, Bimetallic Pd-Cu catalysts for selective CO2 hydrogenation to methanol, *Appl. Catal. B Environ.*, 2015, **170–171**, 173–185.

35 Megha, K. Mondal, T. K. Ghanty and A. Banerjee, Adsorption and Activation of CO2on Small-Sized Cu-Zr Bimetallic Clusters, *J. Phys. Chem. A*, 2021, **125**, 2558–2572.

36 A. Muthuperiyanayagam, A. G. Nabi, D. Di, M. E. Road, U. Kingdom, A. Mathematics, P. O. Nilore, J. J. Road and C. Authors, Adsorption , activation , and conversion of carbon dioxide on small copper-tin nanoclusters, 1–16.

37 M. Kabir, A. Mookerjee and A. K. Bhattacharya, Structure and stability of copper clusters: A tight-binding molecular dynamics study, *Phys. Rev. A - At. Mol. Opt. Phys.*, 2004, **69**, 1–10.

38 C. Vázquez-Vázquez, M. Bañobre-López, A. Mitra, M. A. López-Quintela and J. Rivas, Synthesis of small atomic copper clusters in microemulsions, *Langmuir*, 2009, **25**, 8208–8216.

39 H. Häkkinen, M. Moseler, O. Kostko, N. Morgner, M. A. Hoffmann and B. V. Issendorff, Symmetry and electronic structure of noble-metal nanoparticles and the role of relativity, *Phys. Rev. Lett.*, 2004, **93**, 1–4.

40 J. Kleis, J. Greeley, N. A. Romero, V. A. Morozov, H. Falsig, A. H. Larsen, J. Lu, J. J. Mortensen, M. Dułak, K. S. Thygesen, J. K. Nørskov and K. W. Jacobsen, Finite Size Effects in Chemical Bonding: From Small Clusters to Solids, *Catal. Letters*, 2011, **141**, 1067–1071.

41 N. Austin, J. Ye and G. Mpourmpakis, CO2 activation on Cu-based Zr-decorated nanoparticles, *Catal. Sci. Technol.*, 2017, **7**, 2245–2251.

42 N. Austin, B. Butina and G. Mpourmpakis, CO2activation on bimetallic CuNi nanoparticles, *Prog. Nat. Sci. Mater. Int.*, 2016, **26**, 487–492.

43 A. A. Peterson, F. Abild-Pedersen, F. Studt, J. Rossmeisl and J. K. Nørskov, How copper catalyzes the electroreduction of carbon dioxide into hydrocarbon fuels, *Energy Environ. Sci.*, 2010, **3**, 1311–1315.

44 J. Rossmeisl, Z. W. Qu, H. Zhu, G. J. Kroes and J. K. Nørskov, Electrolysis of water on oxide surfaces, *J. Electroanal. Chem.*, 2007, **607**, 83–89.

45 C. J. Pickard and R. J. Needs, Ab initio random structure searching, *J. Phys. Condens. Matter*, 2011, **23**, 53201.

46 Y. Xu, F. Li, A. Xu, J. P. Edwards, S. F. Hung, C. M. Gabardo, C. P. O'Brien, S. Liu, X. Wang, Y. Li, J. Wicks, R. K. Miao, Y. Liu, J. Li, J. E. Huang, J. Abed, Y. Wang, E. H. Sargent and D. Sinton, Low coordination number copper catalysts for electrochemical CO2 methanation in a membrane electrode assembly, *Nat. Commun.*, 2021, **12**, 4–10.

47 G. Kresse and J. Furthmüller, Efficient iterative schemes for ab initio total-energy calculations using a plane-wave basis set, *Phys. Rev. B - Condens. Matter Mater. Phys.*, 1996, **54**, 11169–11186.

48 K. Mathew, R. Sundararaman, K. Letchworth-Weaver, T. A. Arias and R. G. Hennig, Implicit solvation model for density-functional study of nanocrystal surfaces and reaction pathways, *J. Chem. Phys.*, 2014, **140**, 84106.

49 H. Li, Y. Y. Shen, H. N. Du, J. Li, H. X. Zhang and C. X. Xu, Insight into the mechanisms of CO2 reduction to CHO over Zr-doped Cu nanoparticle, *Chem. Phys.*, , DOI:10.1016/j.chemphys.2020.111012.

50 F. C. Chuang, C. Z. Wang and K. H. Ho, Structure of neutral aluminum clusters Aln (2≤n≤23): Genetic algorithm tight-binding calculations, *Phys. Rev. B - Condens. Matter Mater. Phys.*, 2006, **73**, 125431.

51 H. Y. Mao, B. X. Li, W. F. Ding, Y. H. Zhu, X. X. Yang, C. Y. Li and G. X. Ye, Theoretical study on the aggregation of copper clusters on a liquid surface, *Materials (Basel).*, , DOI:10.3390/ma122333877.

52 D. Y. Shin, J. S. Won, J. A. Kwon, M. S. Kim and D. H. Lim, First-principles study of copper nanoclusters for enhanced

electrochemical CO2 reduction to CH4, *Comput. Theor. Chem.*, 2017, **1120**, 84–90.

53 C. Vogt, M. Monai, E. B. Sterk, J. Palle, A. E. M. Melcherts, B. Zijlstra, E. Groeneveld, P. H. Berben, J. M. Boereboom, E. J. M. Hensen, F. Meirer, I. A. W. Filot and B. M. Weckhuysen, Understanding carbon dioxide activation and carbon–carbon coupling over nickel, *Nat. Commun.*, 2019, **10**, 1–10.